AGU PUBLICATIONS

JGR

Journal of Geophysical Research: Oceans

RESEARCH ARTICLE

10.1002/2013JC009295

Oceanic heat delivery via Kangerdlugssuaq Fjord to the south-east Greenland ice sheet

Mark E. Inall[1], Tavi Murray[2], Finlo R. Cottier[1], Kilian Scharrer[2,3], Timothy J. Boyd[1], Karen J. Heywood[4], and Suzanne L. Bevan[2]

[1]Scottish Association for Marine Science, Scottish Marine Institute, Argyll, UK, [2]Swansea University, Swansea, UK, [3]Now at Enveo IT GmbH, Innsbruck, Austria, [4]University of East Anglia, School of Environmental Science, Norwich, UK

Key Points:
- Ocean heat flux toward the ice sheet is 10 times the previously reported value
- Heat delivered to the calving front is equivalent to ~10 m d^{-1} melt
- Polar Surface Waters melted a substantial volume of ice within the fjord

Correspondence to:
M. E. Inall,
mark.inall@sams.ac.uk

Citation:
Inall, M. E., T. Murray, F. R. Cottier, K. Scharrer, T. J. Boyd, K. J. Heywood, and S. L. Bevan (2014), Oceanic heat delivery via Kangerdlugssuaq Fjord to the south-east Greenland ice sheet, *J. Geophys. Res. Oceans*, *119*, doi:10.1002/2013JC009295.

Received 23 JULY 2013
Accepted 31 DEC 2013
Accepted article online 7 JAN 2014

Abstract Acceleration of the Greenland Ice Sheet (GrIS) tidewater outlet glaciers has increased the ice sheet's contribution to global sea level rise over the last two decades. Coincident increases in atmospheric temperatures around Greenland explain some of the increased ice loss, but warm Atlantic-origin water (AW) is increasingly recognized as contributing to the accelerating ice-mass loss, particularly, via the outlet glaciers of south-east (SE) Greenland. However, there remains a lack of understanding of the variability in heat content of the water masses found to the east of Greenland and how this heat is communicated to the outlet glaciers of the GrIS. Here a new analysis is presented of ocean/GrIS interaction in which the oceanic heat flux toward the ice sheet in Kangerdlugssuaq Fjord (0.26 TW) is an order-of-magnitude greater than that reported for the other major outlet glacier of SE Greenland (Helheim). Heat delivered by AW to the calving front of Kangerdlugssuaq is equivalent to ~10 m d^{-1} melt (i.e., 30–60% of the ice flow speed), and thus is highly significant. During the observational campaign in September 2010 warm Polar Surface Water (PSWw) melted a substantial volume of ice within the fjord; equivalent to 25% of the volume melted by AW alone. Satellite-derived sea surface temperatures show large interannual variability in PSWw over the 20 year period 1991–2011. Anomalously warm PSWw was observed within the fjord prior to the well-documented major ice front retreats of May 2004 and November 2010.

1. Introduction

The recent contribution of the Greenland ice sheet (GrIS) to global sea level rise has doubled through accelerations in the flow speeds of its outlet glaciers [*Rignot and Kanagaratnam*, 2006; *Rignot and Mouginot*, 2012]. These accelerations started in 1998 at Jakobshavn Isbræ in south-west Greenland and later in SE Greenland; 2001 at Helheim, and 2004 at Kangerdlugssuaq [*Luckman and Murray*, 2005; *Rignot and Kanagaratnam*, 2006; *Seale et al*., 2011]. Of the SE Greenland ice sheet, approximately 40% drains, in roughly equal measures, through two major glacier/fjord systems: Kangerdlugssuaq and Helheim/Sermilik (Figure 1). For simplicity, the two glaciers will be referred to as KGG (Kangerdlugssuaq glacier) and HH (Helheim glacier), and their associated fjords as KGF (Kangerdlugssuaq Fjord) and SF (Sermilik Fjord), respectively, throughout this paper. The flow speed of KGG increased from 16 m d^{-1} in 2000 to 33 m d^{-1} in 2005 [*Rignot and Kanagaratnam*, 2006], subsequently reducing to 22 m d^{-1} in 2010 [*Bevan et al*., 2012], whilst HH flow speeds have been somewhat lower and less variable [*Seale et al*., 2011].

Rising air temperatures may well be an important factor in accounting for ice sheet accelerations across SE Greenland, with a regional rise of +3°C from 1981 to 2005 [*Rignot and Kanagaratnam*, 2006]. However, relatively warm Atlantic-origin water masses (AW) occupy the continental margins of both SE and SW Greenland, and their influence is now thought to play an important role in GrIS dynamics [*Christoffersen et al*., 2011; *Rignot et al*., 2012]. One study noted "a striking correspondence between ocean warming and dramatic accelerations and retreats of key Greenland outlet glaciers" [*Hanna et al*., 2009]. Furthermore, glaciers of eastern Greenland located north of the Denmark Strait (north of 69°N), a region where AW is absent from the shelf, have not experienced the rapid retreats seen in the SE Greenland glaciers from the mid-1990s until 2005 [*Seale et al*., 2011].

During the last century, water temperatures to the west of Greenland have been rising at a rate of approximately 0.2°C/decade, associated with an increase in the temperature of inflowing AW into the West Greenland Current [*Zweng and Munchow*, 2006]. The rapid retreat of Jakobshavn Isbræ in 1998 was shown

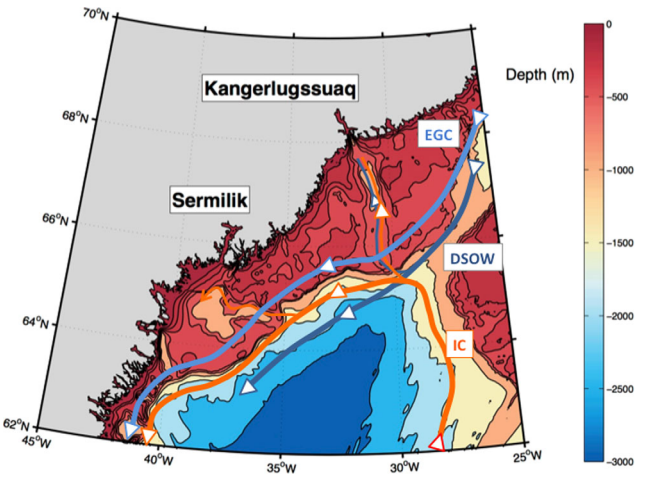

Figure 1. Location map with ETOPO1 bathymetry of the SE Greenland shelf. Contours are at 100 m intervals to 500 m and at 500 m intervals thereafter. Schematic arrows show indicative paths of the East Greenland Current (EGC), the Irminger Current (IC), and the Denmark Strait Overflow Water (DSOW).

to be coincident with a rapid rise in the temperature of AW to the west of Greenland [*Holland et al*., 2008; *Luckman and Murray*, 2005]. The situation in SE Greenland is less clear and no such coincidence between AW temperature rise and glacier retreat has emerged. Whilst there is evidence of a gradual warming trend in AW on the eastern side of the Reykjanes Ridge in the Iceland Basin [*Sarafanov et al*., 2007; *Thierry et al*., 2008] (+1.41°C, 1996–2003), further downstream on the flanks of the SE Greenland shelf there is no significant trend reported for the volume flux of warm AW to the east of Greenland [*Daniault et al*., 2011], and there are no published time series of AW heat content change on the SE Greenland shelf.

It is one thing for AW to be found on the Greenland continental shelf, and quite another for AW to be able to influence the mass balance and dynamics of the ice sheet. In contrast to the proposed mechanism behind the retreat of Jakobshavn Isbræ in SW Greenland, AW heat delivery from the continental shelf to the GrIS in Sermilik Fjord of SE Greenland has been demonstrated to be rather modest at 0.029 TW [*Sutherland and Straneo*, 2012]. Water property analysis of another major outlet glacier system of SE Greenland, KGF, has however received considerably less attention in the literature [*Azetsu-Scott and Tan*, 1997; *Christoffersen et al*., 2011], and the oceanic heat transport along KGF to the GrIS has not hitherto been quantified. Despite a natural tendency to suppose that Sermilik Fjord may be a good exemplar for many the SE Greenland fjordic systems, we show that there are good reasons to anticipate a greater connection between the shelf-resident AW waters and the GrIS in Kangerdlugssuaq Fjord than in Sermilik Fjord.

1.1. Shelf-Resident Water Masses of SE Greenland

The water masses on the SE Greenland shelf are of either Atlantic or Arctic origin (Table 1). There exist three broad definitions for the water masses that are of predominantly Arctic origin. Polar Intermediate Water (PIW) is the densest of these, originating from the colder parts of the Arctic thermocline, and has $\sigma_\theta > 27.7$ and $T < 0$°C. Polar Surface Water (PSW) is less dense than PIW, with $\sigma_\theta < 27.7$ but can be colder and fresher. PSW is warmed and further freshened as it flows south along the SE Greenland shelf, forming warm PSW (PSWw). PSWw can be defined rather broadly as a shelf-resident water mass flowing from the Arctic and Nordic seas associated with the fast (~20 cm s^{-1}) East Greenland Current (EGC), with $\sigma_\theta < 27.7$ and $T > 0$°C [*Rudels et al*., 2002], which may be responsible for up to 50% of the freshwater export from the Arctic through the Fram Strait. South of Denmark Strait the East Greenland Coastal Current (EGCC), a largely seasonal feature [*Sutherland and Pickart*, 2008], becomes increasingly distinct from the EGC as low-salinity coastal jet fed by freshwater from SE Greenland. Temperature and salinity properties of PSWw are therefore strongly modulated by seasonal cycles of solar radiation, and seasonal and interannual variations in sea ice growth and melt. Indeed, the variability in PSWw is strongly seasonal and in some years it can be absent entirely [*Azetsu-Scott and Tan*, 1997; *Christoffersen et al*., 2011; *Dowdeswell et al*., 2008]. The presence or absence of PSWw on the SE Greenland shelf has been explained in two ocean/glacier numerical model simulations through interannual variations in the alongshore wind patterns and heat exchange with the atmosphere [*Christoffersen et al*., 2011]. It is apparent that these three Arctic-origin water masses on the SE Greenland shelf (PIW, PSW, PSWw) are poorly documented and their role in ocean/glacier interactions is not well understood.

Beneath the three Arctic-origin water masses lie the waters of Atlantic origin, commonly and collectively referred to as Atlantic Water (AW). The properties of AW are more tightly defined than those of Arctic-origin

Table 1. Water Mass Definitions and Characteristic Temperature, Salinity, Density, and Depth Ranges Within the Fjord, and Characteristic Temperature, Salinity, Density Ranges of the Shelf-Resident Water Masses

		Characteristic			
Water Mass		T (°C)	S	σ_θ	z
Fjord					
Warm Polar Surface Water	PSWw	>0		<27.7	0–80
Glacial Meltwater	GMW			<24.0	80–250
Modified Atlantic Water	AWm	1.0–4.5	34.4–34.8		250–500
Denmark Strait Overflow Water	DSOW	>0	34.8–34.9	>27.8	>500
Shelf					
Atlantic Water	AW	4.5–6.5	34.8–35.1		
Polar Surface Water	PSW			<27.7	
Polar Intermediate Water	PIW	< 0		>27.7	

surface waters, with $4.5°C < T < 6.5°C$ and $34.8 < S < 35.1$ [*Sutherland and Pickart*, 2008]. AW is identified beyond the shelf break by a temperature maximum and potential vorticity minimum at depth (typically at 200 m at the latitude of KGF and SF) [*Thierry et al*., 2008]. AW is advected southward along the SE Greenland continental margin by the Irminger Current, part of the North Atlantic subpolar gyre recirculating cyclonically around the rim of the Irminger Basin. AW is modified into what may be called AWm (modified, cooler, and fresher) as it is topographically steered toward the coast along wide glacially carved, cross-shelf canyons [*Murray et al*., 2010; *Sutherland and Cenedese*, 2009].

The densest water mass encountered on the SE Greenland shelf is Denmark Strait Overflow Water (DSOW, $\sigma_\theta > 27.8$, $T > 0°C$, and $34.8 < S < 34.9$), which is known to periodically impinge on to the shelf [*Magaldi et al*., 2011] but has not previously been identified within SE Greenland fjordic basins, as it is here.

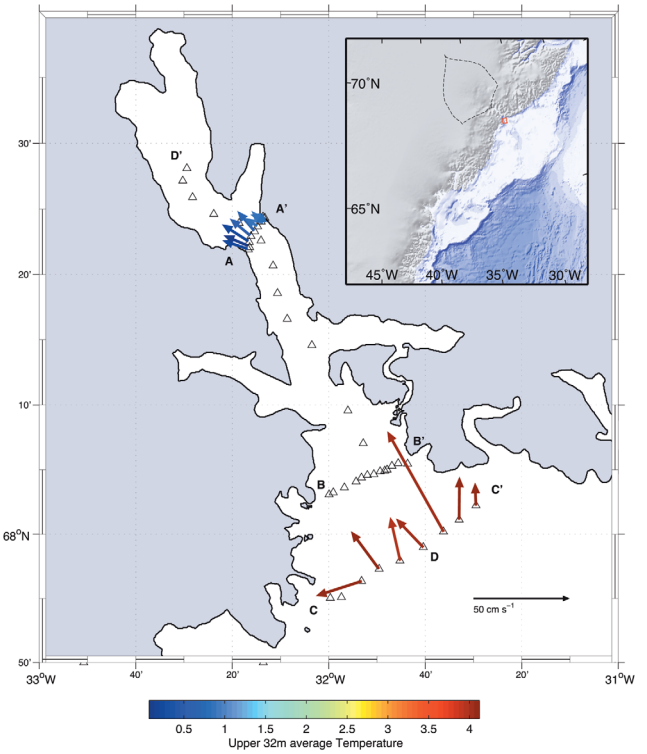

Figure 2. Kangerdlugssuaq Fjord, showing: Section AA′ (max depth = 780 m), BB′ (max depth = 895 m), CC′ (Sill Section, max depth = 550 m), DD′ (along fjord section). Detailed Kangerdlugssuaq Fjord bathymetry is shown in Figure 3, and adjacent shelf bathymetry in Figure 1. Vector arrows show measured absolute velocity current vectors averaged between 8 and 32 m, colored by temperature averaged between the same levels. The insert shows the ice sheet catchment area of Kangerdlugssuaq glacier (dashed line).

1.2. Geometry of the SE Greenland Shelf

KGF (Figures 2 and 3) is a relatively wide (8–10 km) steep-sided, deep (900 m) inlet, approximately 75 km long from the main glacier front to a deep sill (550 m) situated at its broad coastal mouth [*Azetsu-Scott and Tan*, 1997; *Dowdeswell et al*., 2008]. Bathymetric maps show that the deep and wide entrance to KGF extends seaward as a straight and deep trough right across the continental shelf [*Dowdeswell et al*., 2010] (Figure 3). Sermilik, on the other hand, has considerably more complex entrance geometry [*Schjoth et al*., 2012; *Sutherland et al*., 2013] (Figure 1). Direct communication between Sermilik Fjord and the shelf is limited to a deep (600 m) but very narrow channel (<2 km) on the eastern side, and a wider (~6 km) but shallower (~400 m) channel on the western side. A shallow (200 m) partial sill sited

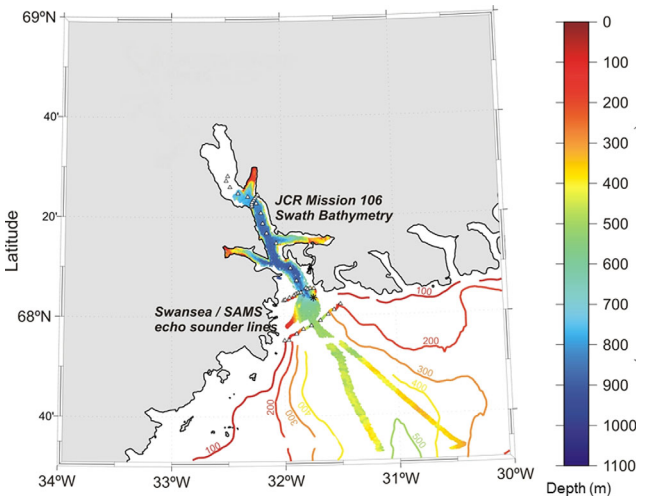

Figure 3. Best available bathymetric data for the Kangerdlugssuaq Fjord and adjacent shelf system. Data are combined from RSS James Clarke Ross swath bathymetry survey of 2004 [*Dowdeswell et al.*, 2010], sounding made during the survey reported in this article, and ETOPO1 global bathymetry (colored contours outside the fjord).

between the two channels effectively blocks the free passage of water between the shelf and the fjord at the depths of AWm through all but the narrow eastern channel, although there is evidence which shows a detailed bathymetric knowledge of this region is still incomplete [*Sutherland et al.*, 2013]. In further contrast to KGF, neither of the Sermilik entrance channels connect directly to a linear cross-shelf trough (see Figure 1). Therefore, the connectivity of the two systems to shelf-resident AWm may be qualitatively and quantitatively different. Consequently, we anticipate that the influence of AWm on glacial dynamics may differ between SF and KGF; certainly, the retreat of Kangerdlugssuaq glacier in 2004–2005 was more marked than the retreat of Helheim glacier during the same period [*Seale et al.*, 2011], although this may be related to internal glacier processes rather than to oceanic heat delivery.

1.3. Motivation

The motivation behind this study, therefore, was to quantify the influence of the shelf-resident water masses on the tidewater glacier of the Kangerdlugssuaq system, particularly on the ice melt within the fjord. A field campaign in September 2010 was designed to allow the required horizontal heat transport and the vertical heat fluxes to be estimated, and the findings of that campaign are reported here. The article is structured as follows: in section 2, the observations are described and methodologies for determining horizontal velocities and vertical heat fluxes are presented, including a consideration of baroclinic seiching. Section 3 describes the along-axis TS structure of the fjord. Estimated along-channel velocities and a circulation scheme consistent with the TS structure are presented in section 4. Section 5 takes the fluxes and the TS distribution to derive heat transports and to quantify a layer-wise heat budget for KGF. Section 6 is a discussion of the primary findings, and concludes the paper.

2. Methods: Vertical Fluxes and Horizontal Velocities

The sampling programme in KGF during September 2010 consisted of full-depth vertical CTD profiling (conductivity, temperature and depth), full-depth shear microstructure vertical profiling, and a 300 kHz vessel mounted Acoustic Doppler Current Profiler (ADCP). Three cross-fjord sections (AA′, BB′, and CC′) and one along-axis section (DD′) were completed, comprising in total forty-nine full-depth microstructure and CTD profiles (Figure 2).

2.1. Diffusivity Estimation From Shear Microstructure

A standard methodology was used for measuring the rate of dissipation of turbulent kinetic energy (ε, unit W kg^{-1}) from the free-fall MSS90 profiler measurements of velocity shear microstructure [*Prandke and Stipps*, 1998]. This methodology involves time series measurements at 416 Hz of velocity shear from the near surface to the seabed from a loosely tethered probe free falling at a speed of 0.8 m s^{-1}. Two microstructure sensors mounted at the front of the probe resolve vertical shear in the horizontal velocity from scales of approximately 0.005–0.5 m. Variance of the shear, $\overline{\left(\frac{du}{dz}\right)^2}$, is calculated by integrating the shear spectra over the inertial subrange (from 2 to 100 cpm, or to the Kolmogorov wave number, whichever is the lower of the two). Shear variance is calculated for 2 m long segments of data (approximately, 2.5 s of data, or 1000 data points) with a 50% overlap between adjacent calculations. Estimates of the dissipation

rate of turbulent kinetic energy are derived using the relationship for isotropic turbulence $\epsilon = 7.5\mu\overline{\left(\frac{du}{dz}\right)^2}$, where μ is the temperature-dependent dynamic viscosity of seawater, thus giving vertical profiles of ε with a resolution of 1 m, with 50% overlap between adjacent values. Estimates of the vertical eddy diffusivity (K_z) were then made from the vertical profiles of ε by using the well-established relationship of Osborn, $K_z = R_f(\epsilon/N^2)/(1-R_f)$ [*Osborn*, 1980] and a flux Richardson number of $R_f = 0.17$, a value commonly used in geophysical applications [*Shih et al*., 2005]. Profiles of the buoyancy frequency squared (N^2) were calculated on ordered density profiles, further smoothed with a 10 m vertical filter to remove the spurious effect of local static instabilities on the estimates of vertical diffusivity. Error bounds on K_z were estimated using a bootstrapping procedure on the 49 profiles used for the layer-wise heat budgeting [*Rippeth and Inall*, 2002]. We use the derived product of vertical eddy diffusivity (and its error estimate) to constrain a layer-wise heat budget of the fjord; the dissipation profiles themselves will not be discussed further here.

2.2. Tidal Correction of Measured Velocities

Direct velocity estimates made using an ADCP from a moving vessel require two corrections to be applied before they can be treated as steady absolute velocities relative to a fixed earth reference frame. First, the movement of the vessel over the ground must be corrected for, since measurements made are relative to the vessel. This is a standard procedure accomplished here by reference to the attitude and positional information from an Ashtech Global Positioning System (GPS). Second, once corrected for vessel motion, barotropic tidal velocities need to be estimated and removed. For tidal velocity correction, the tidal constituents (M2 and S2) at the entrance to KGF were taken from the Arctic Ocean Tidal Inverse model, AOTIM-5 [*Padman and Erofeeva*, 2004]. These constituents were used to force a barotropic tidal model of the fjord. For the purposes of estimating barotropic tidal velocities, it is sufficient to simplify the fjord geometry of the barotropic tidal model to a rectangular channel of appropriate dimensions. For each measurement station, a prediction was generated of the barotropic tidal currents for the duration of each station (typically 30 min). This tidal correction was applied to the measured earth-referenced velocities for each station. Barotropic tides turned out to be weak, with a maximum value of 1 cm s^{-1}, compared to typical measured near-surface flows of around 20 cm s^{-1}. This methodology resulted in profiles of detided, absolute velocity to a depth of 32 m at each station. Deeper than 34 m acoustic returns from the 300 kHz ADCP were too weak to pass the quality threshold for reliable velocity determination. Under more typical conditions, a 300 kHz ADCP returns reliable velocities to a maximum depth of $\sim$120 m. The truncation of good velocities seen here is attributed to either acoustic absorption in the glacial melt surface layer, or to a lack of acoustic scatterers beneath that, or a combination of both; no instrument fault was detected.

2.3. Geostrophic Velocities and Seiching Motions

Temperature and salinity on Section AA′ (Figures 4 and 5) are used as the basis for an estimation of the along-channel geostrophic velocities. Two cores of warm water are seen on Section AA′, one centered at 40 m and another at 450 m, both banked up toward the eastern side of the channel. The warm cores are associated with PSWw and AWm, respectively, as will be discussed further in the TS analysis of section 3. Above the core of the AWm, salinity varied little in the horizontal, and cross-channel density gradients are dominated by cross-channel temperature variations, even at these relatively low temperatures.

On Section AA′, geostrophic velocities below 50 m were calculated assuming a level of no motion at the sill depth of 550 m, which were then adjusted to ensure salt conservation within the fjord, using the methods described below. The geostrophic method is valid in fjords only under certain conditions and because a major result of this paper relies on the validity of the geostrophic method for estimating the velocity in the core of AWm, it is appropriate to give a detailed justification of the method.

For flow along a channel to be in geostrophic balance, the cross-channel pressure gradient on a given pressure surface must be balanced by the Coriolis force acting to the right (northern hemisphere) of the along-channel flow. For this to be possible, and measurable, the channel must be at least as wide as the Rossby deformation radius, and the pressure gradient field must be steady over a few inertial periods, T_f, ($T_f = 12.94$ h at a latitude of 69°N). A third requirement for geostrophic flow in a channel is that an along-channel pressure gradient (or some other driving force) exists to drive the flow. Following the standard methodology [*Chelton et al*., 1998], the mean Rossby radius in KGF on Section AA′ was calculated to be 7.3 km. KGF is considerably wider than this at the mouth (14 km), and remains approximately one Rossby radius wide through

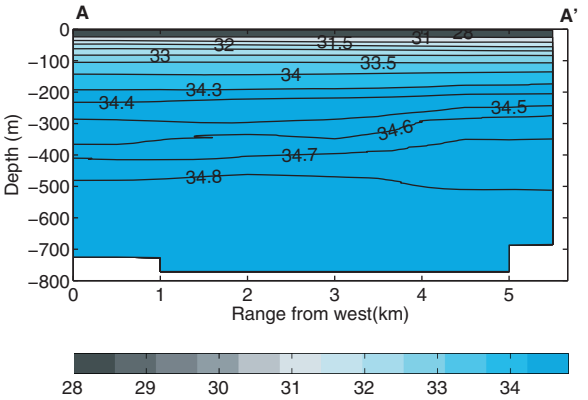

Figure 4. Observed salinity structure on cross-fjord Section AA′. Contour intervals are nonuniform because of the large vertical range near the surface. Contour intervals are: 28, 31, 31.5–33.5 in step of 0.5, and then 34, followed by 34.3–35 in steps of 0.1.

its entire length, and is 6.8 km wide at Section AA′ where geostrophic velocities were estimated. Thus, the first requirement for along-channel geostrophically balanced flow is met.

For the second requirement to be met, that of steadiness of the cross-channel pressure gradient over a few inertial periods, we begin by considering the processes that could temporally modulate the cross-channel density structure such that the observed density structure was the result of aliasing of a higher-frequency process. Seiching motions are commonly found in fjords [*Arneborg and Liljebladh*, 2001] with documented motions dominated by along-channel, low vertical wave number modes. For KGF, the fundamental, so-called "quarter pipe" baroclinic seiche mode, which has a velocity node at the head and antinode at the mouth, has a period of $T = 46$ h; $T = L/4C_1$, where the length of the fjord $L = 75$ km and the mode one baroclinic wave phase speed $C_1 = 1.1$ m s^{-1}, derived here from a dynamical modal analysis of the density structure on Section AA′.

We note that, although Section AA′ took only 8 h to complete, which is a small fraction of the fundamental seiche period, the same station in the middle of Section AA′ was visited on two consecutive days, and measurements made of density structure and upper layer absolute velocity on both occasions separated by 23 h. This time separation between occupations of the same station (23 h) is coincidently exactly half the fundamental seiche period, or exactly $\psi = \pi$ in the notation used in equation (2) (although this coincidence is not important in the analysis which follows). Dynamical modal analysis of the mean vertical density profile on Section AA′ shows that the zero crossing of the horizontal velocity for the first vertical mode is at a depth of $h_1 = 150$ m. Assuming that the vessel mounted ADCP accurately measured the upper layer velocity of the first vertical mode, then from the two visits to the middle of Section AA′ the difference over half a seiche period in both the upper layer velocity (ΔU) and the vertical movement of the isopycnal surface nominally found at 150 m ($\Delta\eta$) are calculated. This is a powerful observation, because seiches are standing waves with velocity and interface displacement at quadrature, and from simple trigonometry it can be shown that by knowing the difference in interface position (i.e., the displacement at 150 m over half a seiche period) and the difference in upper layer velocity, then a solution can be found for both the amplitude of the seiche (displacement and velocity, since they are related by the phase speed and interface depth) and the unknown phase of the seiching motion, $\varnothing$, at which the observations were made. The relationships are:

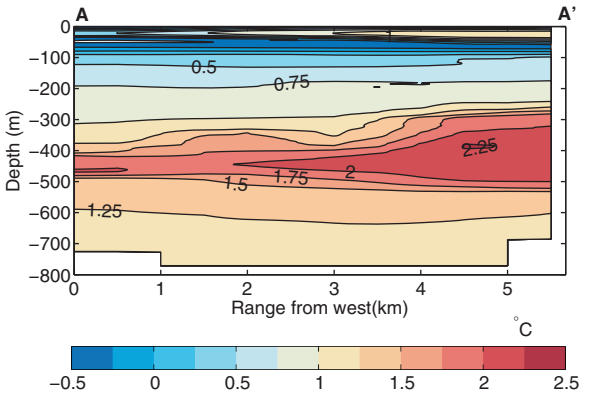

Figure 5. Observed temperature structure on cross-fjord Section AA′. Contour interval throughout is 0.25°C.

$$\tan\varnothing = \frac{\Delta U h_1}{\Delta\eta C_1} \quad (1)$$

and

$$U_0 = \frac{\Delta U}{(\sin(\varnothing+\psi) - \sin\varnothing)} \quad (2)$$

where ΔU is the difference in velocity over half a seiche period in the upper layer velocity, $\Delta\eta$ is the vertical movement of the isopycnal surface nominally found at

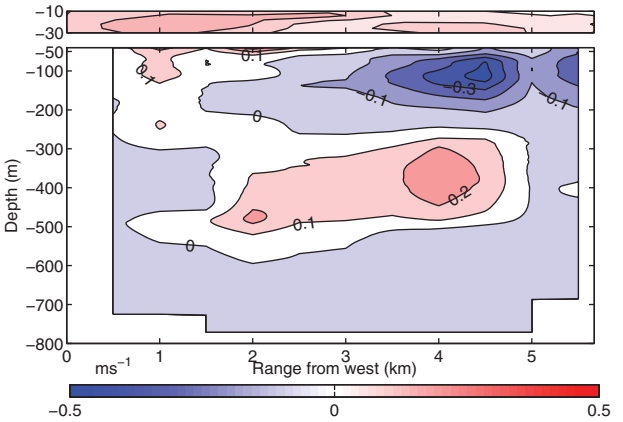

Figure 6. Along-axis velocity in m s^{-1} at Section AA′, (bottom) derived from geostrophy and (top) directly observed using an ADCP. Red colors are positive velocities and into the fjord. Top plot velocities (depth averaged) are represented in Figure 2.

150 m, $\varnothing$ is the unknown phase at which the observations were made, U_0 is the amplitude of the seiche, and ψ the phase difference between occupations. Substituting observed values of $\Delta U = 0.0125$ m s^{-1}, $h_1 = 150$ m, $\Delta\eta = 2.25$ m, $C_1 = 1.1$ m s^{-1}, and $\psi = \pi$ gives $\varnothing = 0.648$ *rad* and $U_0 = 0.01$ m s^{-1}. This demonstrates that there was a very weak first mode along-channel seiche during our occupation of KGF, with a horizontal velocity amplitude of only 1 cm s^{-1}. In itself, an along-channel seiche would not modify the cross-channel density structure. For a seiche to give rise to an across channel density structure observed over a period of 8 h, it would require the presence of an energetic second vertical mode cross-channel seiche. Were this mode to exist it would have a period of about 14 h ($T = W/4C_2$, where $W = 6.8$ km and $C_2 = 0.54$ m s^{-1}; W is the width of the fjord, and C_2 is the mode two baroclinic wave phase speed). It is therefore conceivable that the observed cross-channel density structure could be an artifact of effectively synoptic sampling of an across-basin seiche. However, this is very unlikely, since (a) the more easily energized along-channel seiche was found to be weak, (b) there are no reports in the literature of energetic cross-channel seiching motions in any fjordic systems, and (c) higher vertical modes are invariably less energetic than the fundamental mode. Therefore, we discount the proposition for a synoptic view of an energetic across-fjord seiche to explain the observed density structure during our occupation of KGF, and instead infer that the along-channel density structure was in geostrophic balance with along-channel flows.

2.4. Salt Conservation Constraint

In deriving velocities using the geostrophic method from density profiles on Section AA′, we necessarily make the assumptions of steady frictionless flow with a value of zero flow at some pressure level (the so-called "level of no motion"). There is a further constraint on the velocity field that can be invoked in a closed basin and that is the conservation of salt. Salt is a conserved property where no amount of dilution by meltwater can change the total mass of salt within the system. All salt entering the system, for example, in the deep high-salinity AWm inflow, must leave via a greater volume of less saline outflow. Demanding conservation of salt is a standard oceanographic technique [see e.g., *McDonagh et al*., 2010]. To construct the final velocity section used in the subsequent analyses, and shown in Figure 6, the following technique was adopted: geostrophic velocities were calculated from the bottom to 50 m below the surface, assuming a level of no motion at the sill depth of 550 m. Velocities shallower than 50 m in the surface Ekman layer are typically not in geostrophic balance and this assumption is not made, although in fact the winds were light before and during our occupation of KGF. Instead, the directly measured absolute velocities from 8 to 32 m below the surface were used. The directly measured and geostrophic velocity fields were then merged. A barotropic (depth invariant) adjustment to the geostrophic portion of the velocity field was then derived such that the salt flux through the full section (merged geostrophic and directly measured absolute current) was zero. This adjustment was found, by iteration, to be -3.2 cm s^{-1} and was applied to only the geostrophic portion of the velocity field. This technique is effectively accounting for the uncertainty in the level of no motion by using a robust salt conservation principle.

Having established the methodologies for vertical diffusivity and horizontal velocity estimates, attention now shifts to the TS structure of the fjord, before combining them to derive a heat budget for KGF.

3. Along-Axis TS Structure

Examining the full CTD data set along Section DD′ as a temperature section (Figure 7) and in temperature/salinity (TS) space (Figure 8) reveals a remarkable distribution of water properties. The warmest water mass

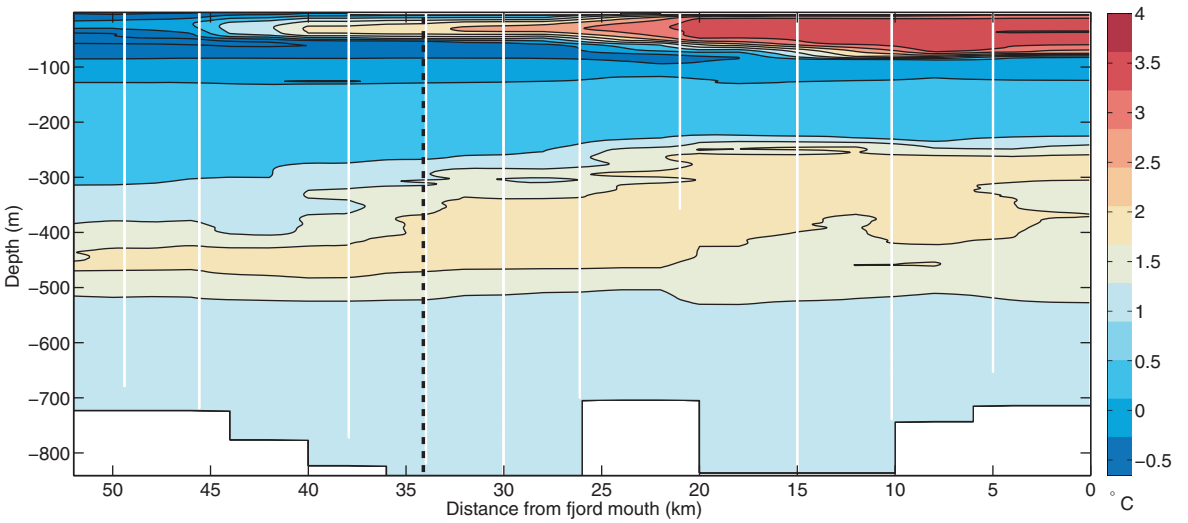

Figure 7. Observed temperature structure on Section DD′ along the axis of KGF, starting from the middle of Section BB′ (0 km) to point D′ (52 km), see Figure 2. Contour interval throughout is 0.5°C. The vertical dashed black line shows the location of Section AA′.

present is PSWw and is found at the fjord mouth and extending for some 30–35 km into the fjord. PSWw resides at the surface from the mouth (X = 0 km) to X = 10 km, glacier ward of this point it becomes capped with a layer of cooler and fresher meltwater. The temperature maximum signature of PSWw cools and freshens uniformly from the mouth to the upper reaches of the fjord, parallel in TS space to an ice-melt mixing line. This would suggest that modification of PSWw is primarily through the melting of ice within the body of the fjord. From a position of about X = 25 km onward (i.e., heading toward the glacier), the fresh, highly stratified surface waters above the PSWw are found to lie increasingly parallel in TS space to a runoff mixing line. This observation suggests modification by direct contact and mixing with fresh runoff, rather than directly with floating ice. With the exception of the sill CTD profile (gray profile, Figure 8), the temperature minimum found beneath the PSWw becomes warmer toward the mouth of the fjord. This temperature minimum is interpreted as the signature of glacial meltwater (GMW), and its down-fjord warming is associated with turbulent mixing with both warmer AWm below, and with warmer PSWw above as the GMW advects seaward and out of the fjord. In TS space, the location of the GMW temperature minimum lies along an approximately straight line, the gradient of which is slightly steeper than the runoff line between GMW and AW. This observation lends direct evidence to support the interpretation that GMW mixes with warmer water masses both above (PSWw) and below (AWm). In contrast, on the sill the gradient in TS space below the GMW temperature minimum corresponds closely to a local ice-melt line, indicative of local TS property modification through melting of icebergs stranded on the sill (grey curve, Figure 8). Beneath the GMW, the temperature maximum of the AWm cools as it penetrates into the fjord basin by about 0.1°C km^{-1} (Figure 7). Beneath the AWm, and landward of the sill, the

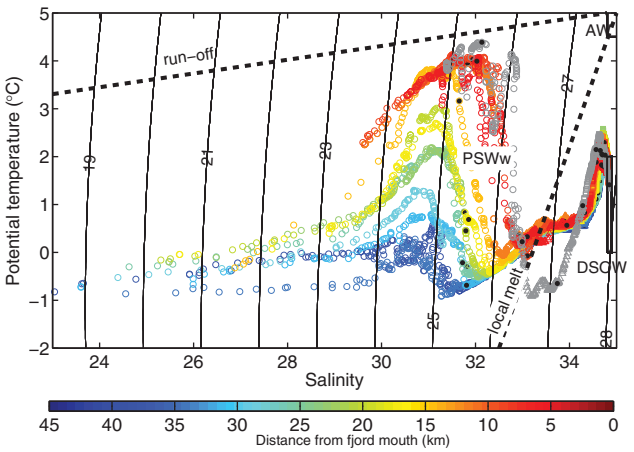

Figure 8. Temperature-Salinity (TS) diagram corresponding to Section DD′ shown in Figure 7. TS profiles are colored by distance along the axis of the in km, starting from the middle of Section BB′ to point D′ (Figure 2). The gray profile is from the middle CTD cast on Section CC′.

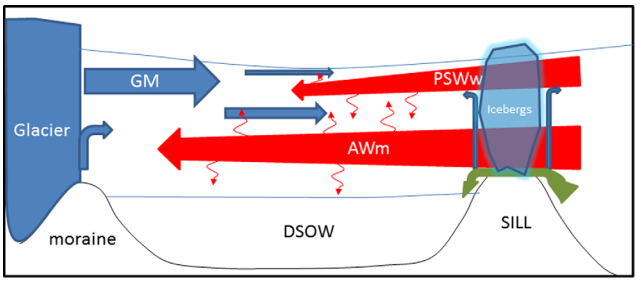

Figure 9. Cartoon of Kangerdlugssuaq Fjord circulation scheme. Blue denotes glacial ice and glacially modified waters. Red denotes warm waters entering from outside the fjord, and green denotes the intermittent inflow of Denmark Strait Overflow Water into the fjord.

basin is filled with DSOW, physically isolated from the shelf waters by the sill. This analysis of the fjord water properties in TS space is fully and independently consistent with the along-axis velocity field estimated for Section AA′ (Figure 6). A four-layered circulation schematic summarizes these findings, and is depicted in cartoon form in Figure 9. This interpretation of a multilayered circulation scheme for this system is consistent with results from a primitive equation model of the same system [*Sole et al*., 2012].

4. Velocity Structure and Circulation Scheme

The proposition therefore is that the layered exchange flows in KGF are driven by (here unidentified) along-channel pressure gradients, which change sign with depth, and because the gradients are steady (over a time period greater than that for geostrophic adjustment, i.e., several inertial periods) the flows they drive achieve a geostrophic balance. We have shown that the fjord is one Rossby deformation radius wide such that the geostrophic balance is manifest in an observable cross-channel pressure gradient field. Turning our attention seaward and onto the wide trough that brings AWm toward the coast, the flow here is likely to be in geostrophic balance also. Toward the glacier, on the other hand, the layered exchange flow must break down completely as AWm is converted into GMW through vigorous convective plume mixing in the vicinity of the calving front, a phenomenon for which there is a body of observational evidence [see e.g., *Jenkins*, 2011, and references therein].

There is further evidence to support the notion of a persistent and steady layered exchange flow in KGF. The only direct velocity estimates published for KGF are from an AUV mission at the mouth of the fjord made during September 2004 from the *RSS James Clarke Ross* (cruise ID JR106) [*Dowdeswell et al*., 2008] and reproduced here (Figure 10). This is relevant to our study because of the similarity in season between the two observing periods and because hydrographic conditions in 2004 were similar to those of 2010 [*Christoffersen et al*., 2011], with PSWw and AWm both present and flowing into the fjord as surface and deep layers, respectively. The AUV section at the mouth of the fjord shows this strong inflow at the depth of AWm, and strong outflow at the depth of GMW.

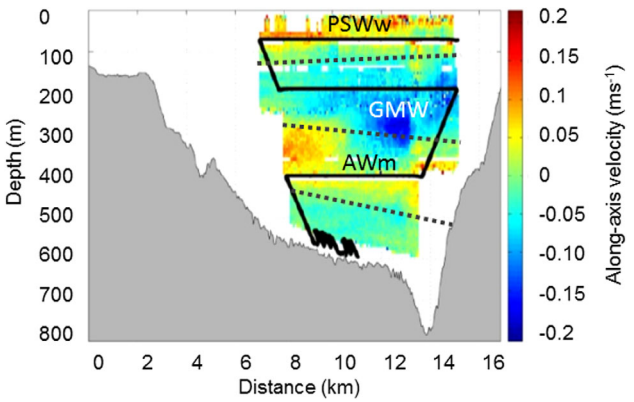

Figure 10. Along-axis absolute velocity section at the mouth of Kangerdlugssuaq measured by an AUV, adapted from *Dowdeswell et al*. [2008] and reprinted from the Journal of Glaciology with permission of the International Glaciological Society.

Evidence that the inflowing AWm at the mouth of KGF penetrated farther into the fjord than the mouth section occupied by the AUV comes from unpublished data from the same expedition. In Figure 11, a temperature profile from a CTD cast and an along-axis detided velocity profile from the vessel mounted 75 kHz ADCP (averaged over 20 min) taken close to the middle station of our Section AA′ clearly reveal a deep two layer counter flowing structure of AWm and GMW. Unfortunately, technical problems with the VMADCP encountered during JR106 prevent a comparison being made with the

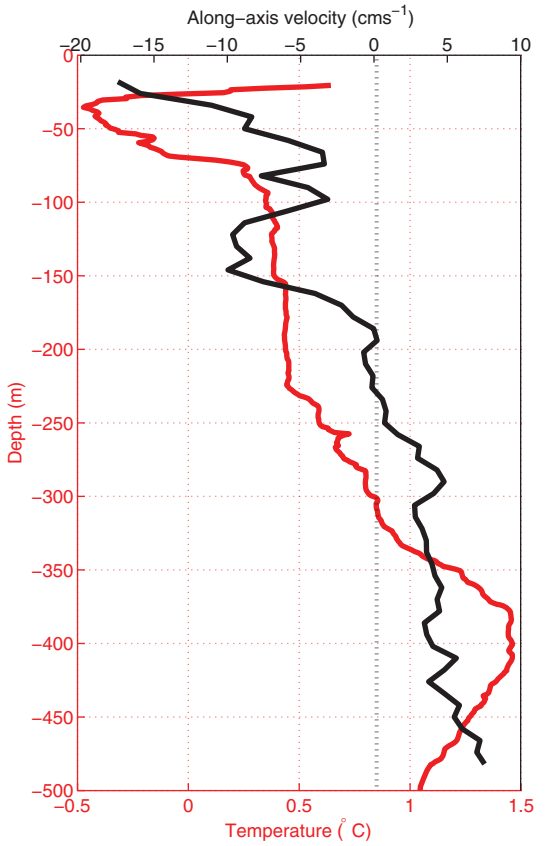

Figure 11. CTD temperature and along-axis velocity profiles from vessel mounted 75 kHz ADCP measured during cruise JCR106b (September 2004). Data are from Station 22 which lies in the center of Section AA′ of this paper.

spatial structure of the velocity field on Section AA′. The flows observed in September 2004 from JR106 are about a factor of two weaker than were observed in 2010, but the temperature of the AWm was also ∼0.5°C cooler, perhaps indicative of weaker driving of the baroclinic exchange in 2004 compared with 2010. Insufficient CTD data exist from JR106 in 2004 to attempt to reconstruct the observed velocities using the geostrophic method described in section 2.

Although not of direct relevance to KGF, further evidence exists which demonstrates that geostrophically balanced baroclinic exchange flows operate in many fjordic systems; both in the arctic (e.g., Petermann [*Johnson et al.*, 2011] and Kongsfjorden [*Svendsen et al.*, 2002]), and subarctic (e.g., the Clyde Sea [*Janzen et al.*, 2005]).

5. Heat Budget

Whilst circulation schemes can be used to quantify the horizontal component of heat and salt fluxes across a given section, the turbulent exchange of heat and salt between layers is traditionally calculated as the residual between two or more sections. As we have seen from section 3, the TS properties of PSWw, GMW, and AWm change considerably as they advect along the axis of the fjord. This implies either significant adiabatic diapycnal turbulent fluxes between layers or diabatic forcing within layers caused by the local melting of icebergs. Both of these processes can modify the T and S of a layer, the former as a down-gradient flux and the latter acting to both cool and freshen. By combining, (a) direct vertical profile measurements of turbulent microstructure within the fjord with, (b) the TS distribution, (c) the observed and geostrophic velocity estimates, and (d) an advective/diffusive balance model for the layer-wise circulation, the horizontal and vertical heat and salt fluxes within the fjord basin can be quantified. The result is the first robust observational picture of circulation and exchange within the fjord. Further, as a residual term, an estimate can be made of the diabatic effects of iceberg melting within the fjord (Table 2).

Table 2. Heat Content Changes of the Layers, Spatially Bounded by Sections AA′ and BB′, Expressed as Watts per Horizontal Unit Area[a]

	Advective Heat Change $H\bar{\rho}C_p\overline{U}\frac{\partial\overline{T}}{\partial x}$ (wm^{-2})	Vertical Heat Flux Divergence $\bar{\rho}C_p\left(K_z\frac{\partial T}{\partial z}\right)$ (wm^{-2})	Residual (Advective-Vertical Divergence) (Wm^{-2})	Melt Rate Within Fjord (Equivalent) (m d^{-1})
(1) PSWw	−105	40 − 18 ± 4.1	−127 ± 4.1	2.50
(2) GMW	+6.6	+42.9 ± 7.8	−36.3 ± 7.8	0.70
(3) AW	−42.0	−61.6 ± 15.9	19.6 ± 15.9	-
(4) DSOW	-	+36.7 ± 3.2	−36.7 ± 3.2	-

[a]This is the heat used to melt ice within the Fjord. Positive values represent a warming of the layer. H is layer thickness, $\overline{U}$, $\overline{T}$, and $\overline{\rho}$ are mean layer velocity, temperature, and density, respectively. Air-sea heat flux (warming of 40 W m^{-2}) is included for PSWw. See text for a description of the terms.

The form of the scalar (T) advection/diffusion equation used here for the heat budget estimation has the form:

$$\frac{\partial T}{\partial t}+u\frac{\partial T}{\partial x}=\frac{1}{\rho}\frac{\partial}{\partial z}\left(\rho K_z\frac{\partial T}{\partial z}\right)+Q_s \tag{3}$$

This may be rewritten for each water mass "layer" as:

$$\underset{A}{\left.\frac{\partial \overline{T}}{\partial t}\right|_L}+\underset{B}{\overline{U}\left.\frac{\partial \overline{T}}{\partial x}\right|_L}=\underset{C}{1\bar{\rho}\frac{1}{H_L}\left[\left(\bar{\rho}K_z\frac{\partial T}{\partial z}\right)|_{(L,L-1)}\right]}+\underset{D}{\left(\bar{\rho}K_z\frac{\partial T}{\partial z}\right)\Big|_{(L,L+1)}\Bigg]}+\underset{E}{Q_s} \tag{4}$$

where, $L = 1$–4 represents the four layers defined as PSWw, GMW, AWm, and DSOW, H_L is the thickness of layer L, and the overbars denote layer averages. The two terms on the LHS of equation (4) (A and B) are the time rate of change and the along-axis advective terms, respectively. The first two terms on the RHS of equation (4) (C and D) are the vertical eddy diffusive fluxes between each layer and the layers above and below, denoted by (L, $L-1$) and (L, $L+1$), respectively. Taken together the first two terms on the RHS are the vertical eddy diffusive heat flux divergence term, resulting in a net heating or cooling of each layer. For the surface layer ($L = 1$, PSWw) and bottom layer ($L = 4$, DSOW), the diffusive terms (L, $L-1$) and (L, $L+1$), respectively, are zero (no vertical eddy diffusive heat flux out of the sea surface or through the seabed). The final term on the RHS of equation (4), Q_s (term E) applies to the surface layer only and is a surface heat flux exchange between $L = 1$ and the atmosphere; it is zero for all other layers. For the purposes of the layer-wise heat budget presented in Table 2, terms in equation (4) have been multiplied by $\overline{\rho}C_pH_L$ to convert from units of K s^{-1} to units of W m^{-2}.

Thus, the terms in the budget (Table 2) represent changes in the heat content of each layer between the control sections AA′ and BB′ expressed as equivalent vertical heat fluxes in units of Watts per unit horizontal surface area. Having obtained the best estimate of the along-fjord velocity field on Section AA′ as shown in Figure 6, the heat budget presented in Table 2 may be understood as follows. Column one assigns the water mass name to each layer. Boundaries between layers are defined with reference to the zero crossings in the section averaged velocity field at Section AA′ as shown in Figure 6. Column two is the total change in the heat content of the layer, expressed as a vertical heat flux (Watts per unit horizontal area), and calculated as the product of the mean layer velocity and the mean horizontal temperature gradient within the layer between Sections AA′ and BB′ (term B in equation (4)). Column three is the measured vertical eddy diffusive heat flux (estimated from the microstructure measurements) summed along both upper and lower boundaries of each layer (terms C and D, equation (4)). At the upper boundary of the surface layer (PSWw), the air-sea heat flux of 40 W m^{-2} (term E, equation (4)) is estimated from bulk formulae using observed sea surface temperature from the CTD profiles, and air temperature and wind speed from the Danish Meteorological Institute met station at the mouth of the fjord (Station ID 04351 at Aputiteeq, 67°32′N 32°18′W [*Carstensen and Jørgensen*, 2011]).

At the boundaries between layers, the vertical heat flux is the turbulent flux driven by turbulent mixing. This turbulent flux is calculated as the product of the vertical eddy diffusivity and the vertical temperature gradient, summed over all the microstructure profiles of, and between, Sections AA′ and BB′. The layer over which the turbulent fluxes are calculated is chosen to be 20 m thick, 10 m either side of the layer boundaries. Individual flux estimates are made for each 1 m value of K_z and $\partial T/\partial Z$, there are thus 20 independent flux estimates for each boundary from each profile, and a bootstrap method is used to give 95% confidence limits to the mean value quoted. There is no flux out of the base of the DSOW layer, which is the seabed. Column four is the residual heat content of each layer (term A in equation (4)), which is the difference between the observed advective heat content change and the total vertical fluxes out of or into each layer (column two minus column three). This is the contribution to the heat budget for each layer from diabatic forcing and represents the heat that is available to melt ice in each layer, or in the case of the DSOW (which is stagnant) available to slowly change the temperature of that layer.

Two forms of ice melt occur: melt within the fjord (of icebergs and sea ice) and ice melt at the glacier front. Heat available to melt ice within the fjord is converted for each layer to an equivalent melt rate of the

glacier front in m d^{-1} for comparison with other studies. This is merely for comparative purposes and does not indicate real melting at the glacier front; for example, PSWw does not directly melt the calving front since it does not extend that far (see Figure 7). A separate calculation is made to quantify the horizontal heat delivery (heat transport) associated with AWm advection toward the glacier through Section AA′ and is computed as the area integral of the product of the geostrophic velocity and the observed temperature in the AWm layer. The AWm temperature is referenced to the mean outflowing temperature of the GMW lying above the AWm. This calculation gives a value of 0.26 TW, which may be converted into a total volume of ice melted per unit time, and then to an equivalent glacier front linear melt rate. The volume of glacial ice melted per unit time can be expressed as, $V = Q/\rho_{ice}(C_{ice}\Delta T + L_f)$; where $Q = 0.26$ TW, $\rho_{ice} = 930$ kg m^{-3}, $C_{ice} = 2100$ J kg^{-1} K^{-1}, $L_f = 334{,}500$ J kg^{-1}, and $\Delta T = 10°C$ is the temperature below freezing point of the glacier, although V is insensitive to ΔT since $L_f > 100 \times C_{ice}$. This yields a melt rate of 831 m^3 s^{-1} or 26.2 km^3 yr^{-1}. Estimating the glacier calving front to have a vertical cross-sectional area of 850 × 8300 m^2 gives an equivalent glacier front linear melt rate of 10.1 m d^{-1}. The equivalent melt rate at the glacier front represented by the heat contained within the AWm is therefore ~30–60% of the ice flow rate at the margin. Whilst, we cannot know whether this is a true representation of the AWm-influenced melt rate at the glacier front, if it is then it has important implications for the calving rate, with a recent modeling study showing linear increase of calving rate with submarine frontal melting [*O'Leary and Christoffersen*, 2013].

The heat transport value of 0.26 TW is a maximal value, since it is derived from the residual heat in AWm available for melting between Section AA′ and the glacier front some 20 km away. It is also a synoptic value estimated during a single field campaign in September 2010. Similarly large (synoptic) heat transports have been reported for Petermann Fjord [*Johnson et al*., 2011] (0.31 TW) and Tor Fjord [*Rignot et al*., 2010] (0.16 TW). The figure of 0.26 TW is an order-of-magnitude larger than the only other estimate for SE Greenland at Sermilik Fjord (0.029 TW) [*Sutherland and Straneo*, 2012]. Furthermore, the volume of ice melted within KGF (equivalent to 3.2 m d^{-1} of glacier retreat and dominated, 2.5 m d^{-1}, by PSWw) is one third of the value of the glacier front melting potential of the AWm.

6. Discussion and Conclusions

In this paper, we have combined a set of turbulent microstructure profiles with standard hydrographic measurements and analysis techniques in one of the two major SE Greenland Fjords. We have demonstrated that: (a) The capacity to deliver warm AWm to the GrIS in KGF is an order-of-magnitude greater than that reported for Sermilik Fjord, the second major fjordic system of SE Greenland [*Sutherland and Straneo*, 2012], (b) PSWw has a substantial capacity to melt ice within the fjord (equivalent to 2.5 m d^{-1} of glacial front retreat) but not directly at the glacier calving front, since it does not penetrate the entire length of the fjord; (c) the volume of ice melted near the glacier front is three times greater than the total melted within the fjord.

It is a somewhat unexpected result that the AWm heat transport in KGF is apparently 10 times that of Sermilik. Comparison with data from 2004, the only other year for which velocity estimates within KGF are available, suggests that the transport of AWm in 2010 was perhaps double that of 2004. The heat transport result presented here depends on geostrophic balance within the AWm and GMW water masses within KGF. This approach has been justified by discounting other reasonable explanations for the observed cross-fjord density structure, nevertheless the fact remains that direct velocity measurements of AWm within KGF remain elusive (with the exception of the 2004 VMADCP profile). If the baroclinic circulation of AWm is driven by an external baroclinic pressure gradient from the greater thickness of AWm on the shelf, then the more topographically open nature of the mouth of KGF (in comparison to SF) may be a determining factor in the apparent difference in heat delivery between the two systems. If, on the other hand, the baroclinic circulation is primarily driven by the available potential energy from the submerged face of a several hundred meter high melting glacier front, then reasons for the apparent difference between the two systems are less clear. Analysis of the driving mechanism(s) of the layered exchange in KGF and SF is beyond the scope of this article, but a necessary next step in better understanding the circulation of SE Greenland's outlet glacier fjords which is beginning to be addressed [*Sciascia et al*., 2013].

Interannual and/or interseasonal variation may also contribute to the apparent differences in heat delivery between KGF and SF. Our measurements derive from data gathered in the late summer during a year when

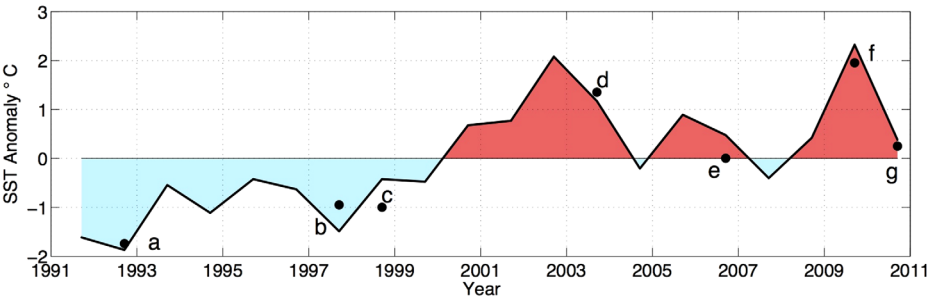

Figure 12. (A)ATSR ((Advanced) Along Track Scanning Radiometer) SST for the mouth region of Kangerdlugssuaq Fjord SE Greenland averaged from September to October plotted as an anomaly from the 20 year average of 1991–2011. Points indicate in situ temperature anomaly (relative to the 20 year ATSR mean) at 2 m water depth from various sources: (a) *Azetsu-Scott and Tan* [1997], (b) *Rudels et al*. [2002], (c and e) ICES database, (d) *Sutherland and Pickart* [2008], and (f and g) our own studies.

PSWw was unusually warm; however, there is no evidence to suggest a strong coupling exists between AWm and PSWw. It might be argued that AWm should lose more heat through vertical mixing to surface waters above in years of cooler PSWw; however, no measurable evidence in support of coupling between AWm temperature and SST has been found [*Sutherland et al*., 2013]. There is evidence in SF that AWm temperature shows modest seasonal variation (warmer in the winter), but whether this may increase or decrease the heat transport is unclear [*Straneo et al*., 2011]. Heat transport estimates quoted for SF (0.029 TW) are derived from observations made in 2008 and 2009, so it remains a possibility that the apparent differences in AWm heat transport between SF and KGF relate simply to the different years of observation, but insufficient data exist to investigate this further.

PSWw, on the other hand, is strongly seasonal, not being present in the winter and spring months. Furthermore, it is possible from satellite-derived SST data to investigate interannual variations in the temperature of PSWw. In situ records show 2004 and 2010 to be years when both SST on the SE Greenland shelf was anomalously high, and PSWw intruded far into KGF [*Christoffersen et al*., 2011]. In situ hydrogrpahic data from SE Greenland are sparse, so to quantify interannual variations in PSWw on the shelf, we use satellite-derived sea surface temperature (SST) as a proxy for PSWw (Figure 12). (A)ATSR ((Advanced) Along Track Scanning Radiometer) SST data for a 20 km square region at the mouth of KGF were averaged from September to October and plotted as an anomaly from the 20 year average of 1991–2011. Available in situ data from a variety of sources are overlaid as anomalies from the 20 year ATSR SST mean. The strongest SST anomalies from the 20 year mean (1991–2011) are seen in late 2003 (+2.1°C), 2004 (+1.3°C), and 2010 (+2.3°C), with the lowest anomaly recorded in 1993 (−1.8°C). These findings reinforce the notion that 2004 and 2010 were unusually warm years with respect to PSWw, coincidentally the 2 years when observations within KGF are available, but we reiterate that there is no evidence to suggest that AWm was similarly anomalously warm. We conclude that on the basis of available data is it not possible to make any meaningful statements on the possible interannual variations of AWm within KGF or other SE Greenland Fjords.

The role of interannual variations in Arctic summer sea ice cover, downstream SE Greenland shelf SSTs, and the concomitant temperature of PSWw do however deserve future attention. The temperature peak of PSWw in 2004 preceded a rapid retreat of the glacial calving front [*Bevan et al*., 2012]. Whilst there is no evidence for causality, one may conjecture that a warm PSWw year may be a contributory mechanism behind reduced buttressing effects at the glacier front by melting the sikkusak on the fjord surface which decreases the apparent resistance to calving at the glacier face, leading to greater calving in following summer. There may therefore be a subtle interplay between AWm heat delivery and PSWw temperature, with a greater efficacy of AWm-induced calving in the year after an anomalously warm PSWw year. This is conjecture, and what has been shown in this article, however, is that in terms of direct melting and undercutting at the calving front AWm is the dominant oceanographic contribution. The results and analysis presented here suggest that ocean processes, such as undercutting of the calving front or reduction of buttressing, are very likely to be important for Kangerdlugssuaq glacier and the south-east Greenland ice sheet.

Acknowledgments
This paper is dedicated to the memory of friend and colleague Tim Boyd. The field campaigns, SLB and KS were funded by Leverhulme Trust Research Leadership Scheme GLIMPSE project. Funding for MEI and FRC from NERC awards (NE/I017704/1 and NE/I030259/1 FASTNEt). MEI would like to thank Elaine McDonagh for advice on salt budget constraints.

References

Arneborg, L., and B. Liljebladh (2001), The internal seiches in Gullmar Fjord. Part II: Contribution to basin water mixing, *J. Phys. Oceanogr.*, *31*(9), 2567–2574.

Azetsu-Scott, K., and F. C. Tan (1997), Oxygen isotope studies from Iceland to an East Greenland Fjord: Behaviour of glacial meltwater plume, *Mar. Chem.*, *56*, 239–251.

Bevan, S. L., A. J. Luckman, and T. Murray (2012), Glacier dynamics over the last quarter of a century at Helheim, Kangerdlugssuaq and 14 other major Greenland outlet glaciers, *Cryosphere*, *6*, 923–937, doi:10.5194/tc-6-923-2012.

Carstensen, L. S., and B. V. Jørgensen (2011), Weather and Climate Data from Greenland 1958–2010, Tech. Rep. 11–10, 1–22 pp., Dan. Meteorol. Inst., Copenhagen.

Chelton, D. B., R. A. DeSzoeke, M. G. Schlax, K. El Naggar, and N. Siwertz (1998), Geographic variability of the first baroclinic Rossby radius of deformation, *J. Phys. Oceanogr.*, *28*, 433–460.

Christoffersen, P., R. I. Mugford, K. J. Heywood, I. Joughin, J. A. Dowdeswell, J. P. M. Syvitski, A. Luckman, and T. J. Benham (2011), Warming of waters in an East Greenland fjord prior to glacier retreat: Mechanisms and connection to large-scale atmospheric conditions, *Cryosphere*, *5*(3), 701–714, doi:10.5194/tc-5-701-2011.

Daniault, N., H. Mercier, and P. Lherminier (2011), The 1992–2009 transport variability of the East Greenland-Irminger Current at 60N, *Geophys. Res. Lett.*, *38*, L07601, doi:10.1029/2011GL046863.

Dowdeswell, J. A., et al. (2008), Autonomous underwater vehicles (AUVs) and investigations of the iceocen interface in Antarctic and Arctic waters, *J. Glaciol.*, *54*(187), 661–672.

Dowdeswell, J. A., J. Evans, and C. O'Cofaigh (2010), Submarine landforms and shallow acoustic stratigraphy of a 400 km-long fjord-shelf-slope transect, Kangerlussuaq margin, East Greenland, *Quat. Sci. Rev.*, *29*(25–26), 3359–3369.

Hanna, E., J. Cappelen, X. Fettweis, P. Huybrechts, A. Luckman, and M. H. Ribergaard (2009), Hydrologic response of the Greenland ice sheet: The role of oceanographic warming, *Hydrol. Processes*, *23*(1), 7–30, doi:10.1002/hyp.7090.

Holland, D. M., R. H. Thomas, B. De Young, M. H. Ribergaard, and B. Lyberth (2008), Acceleration of Jakobshavn Isbrae triggered by warm subsurface ocean waters, *Nat. Geosci.*, *1*(10), 659–664, doi:10.1038/ngeo316.

Janzen, C., J. H. Simpson, M. E. Inall, and F. R. Cottier (2005), Cross-sill exchange and frontal flows over the sill of a broad fjord, *Cont. Shelf Res.*, *25*, 1805–1824.

Jenkins, A. (2011), Convection-driven melting near the grounding lines of ice shelves and tidewater glaciers, *J. Phys. Oceanogr.*, *41*, 2270–2294.

Johnson, H. L., A. Munchow, K. K. Falkner, and H. Melling (2011), Ocean circulation and properties in Petermann Fjord, Greenland, *J. Geophys. Res.*, *116*, C01003, doi:10.1029/2010JC006519.

Luckman, A., and T. Murray (2005), Seasonal variation in velocity before retreat of Jakobshavn Isbræ, Greenland, *Geophys. Res. Lett.*, *32*, L08501, doi:10.1029/2005GL022519.

Magaldi, M. G., T. W. N. H. Haine, and R. S. Pickart (2011), On the nature and variability of the East Greenland Spill Jet: A case study in summer 2003, *J. Phys. Oceanogr.*, *41*(12), 2307–2327.

McDonagh, E. L., P. MeLeod, B. A. King, H. L. Bryden, and S. Torres-Valdes (2010), Circulation, heat and freshwater transport at 36°N in the Atlantic, *J. Phys. Oceanogr.*, *40*, 2661–2678, doi:10.1175/2010JPO4176.1.

Murray, T., et al. (2010), Ocean regulation hypothesis for glacier dynamics in southeast Greenland and implications for ice sheet mass changes, *J. Geophys. Res.*, *115*, F03026, doi:10.1029/2009JF001522.

O'Leary, M. O., and P. Christoffersen (2013), Calving on tidewater glaciers amplified by submarine frontal melting, *Cryosphere*, *7*, 119–128, doi:10.5194/tc-7–119-2013.

Osborn, T. R. (1980), Estimates of the local rate of vertical diffusion from dissipation measurements, *J. Phys. Oceanogr.*, *10*, 83–89.

Padman, L., and S. Erofeeva (2004), A barotropic inverse tidal model for the Arctic Ocean, *Geophys. Res. Lett.*, *31*, L02303, doi:10.1029/2003GL019003.

Prandke, H., and A. Stipps (1998), A microstructure profiler to study mixing and turbulent transport processes, *IEEE OCEANS 1998 Conference Proceedings*, *1*, 179–183, doi: 10.1109/OCEANS.1998.725732.

Rignot, E., and P. Kanagaratnam (2006), Changes in the velocity structure of the Greenland Ice Sheet, *Science*, *311*, 986–990, doi:10.1126/science.1121381.

Rignot, E., and J. Mouginot (2012), Ice flow in Greenland for the International Polar Year 2008–2009, *Geophys. Res. Lett.*, *39*, L11501, doi:10.1029/2012GL051634.

Rignot, E., M. Koppes, and I. Velicogna (2010), Rapid submarine melting of the calving faces of West Greenland glaciers, *Nat. Geosci.*, *3*(3), 187–191, doi:10.1038/ngeo765.

Rignot, E., I. Fenty, D. Menemenlis, and Y. Xu (2012), Spreading of warm ocean waters around Greenland as a possible cause for glacier acceleration, *Ann. Glaciol.*, *53*(60), 257–266, doi:10.3189/2012aog60a136.

Rippeth, T. P., and M. E. Inall (2002), Observations of the internal tide and associated mixing across the Malin Shelf, *J. Geophys. Res.*, *107*(C4), 3028, doi:3028 10.1029/2000jc000761.

Rudels, B., E. Fahrbach, J. Meincke, G. Budéus, and P. Eriksson (2002), The East Greenland Current and its contribution to the Denmark Strait overflow, *ICES J. Mar. Sci.*, *59*, 1133–1154.

Sarafanov, A., A. Sokov, A. Demidov, and A. Falina (2007), Warming and salinification of intermediate and deep waters in the Irminger Sea and Iceland Basin in 1997–2006, *Geophys. Res. Lett.*, *34*, L23609, doi:10.1029/2009GL031074.

Schjoth, F., C. S. Andresen, F. Straneo, T. Murray, and K. Scharrer (2012), Campaign to map the bathymetry of a major Greenland fjord, *EOS Trans. AGU*, *93*(14), 141–152.

Sciascia, R., F. Straneo, C. Cenedese, and P. Heimbach (2013), Seasonal variability of submarine melt rate and circulation in an East Greenland fjord, *J. Geophys. Res.*, *118*, 2492–2506, doi:10.1002/jgrc.20142.

Seale, A., P. Christoffersen, G. Mugford, and M. O'Leary (2011), Ocean forcing of the Greenland Ice Sheet: Calving fronts and oatterns of retreat identified by automatic satellite monitoring of eastern outlet glaciers, *J. Geophys. Res.*, *116*, F03013, doi:10.1029/2010JF001847.

Shih, L. H., J. R. Koseff, G. N. Ivey, and J. H. Ferziger (2005), Parameterisation of turbulent fluxes and scales using homogeneous sheard stratified turbulence simulations, *J. Fluid Mech.*, *525*, 193–214, doi:10.1017/S0022112004002587.

Sole, A. J., J. Payne, P. W. Nienow, P. Christoffersen, F. R. Cottier, and M. E. Inall (2012), Increased glacier runoff enhances the penetration of warm Atlantic water into a large Greenland fjord, *Cryosphere Discuss.*, *6*, 4861–4896, doi:10.5194/tcd-6-4861-2012.

Straneo, F., R. G. Curry, D. A. Sutherland, G. S. Hamilton, C. Cenedese, K. Vage, and L. A. Stearns (2011), Impact of fjord dynamics and glacial runoff on the circulation near Helheim Glacier, *Nat. Geosci.*, *4*(5), 322–327, doi:10.1038/ngeo1109.

Sutherland, D. A., and C. Cenedese (2009), Laboratory experiments on the interaction of a buoyant coastal current with a canyon: Application to the East Greenland Current, *J. Phys. Oceanogr.*, *39*, 1258–1271, doi:10.1175/2008JPO4028.1.

Sutherland, D. A., and R. S. Pickart (2008), The East Greenland Coastal Current: Structure, variability, and forcing, *Prog. Oceanogr.*, *78*(1), 58–77, doi:10.1016/j.pocean.2007.09.006.

Sutherland, D. A., and F. Straneo (2012), Estimating ocean heat transports and submarine melt rates in Sermilik Fjord, Greenland, using lowered acoustic Doppler current profiler (LADCP) velocity profiles, *Ann. Glaciol.*, *53*(60), 50–58, doi:10.3189/2012AoG60A050.

Sutherland, D. A., F. Straneo, G. B. Stenson, F. J. M. Davidson, and M. O. Hammill (2013), Atlantic water variability on the SE Greenland continental shelf and its relationship to SST and bathymetry, *J. Geophys. Res.*, *118*, 847–855, doi:10.1029/2012JC008354.

Svendsen, H., et al. (2002), The physical environment of Kongsfjorden-Krossfjorden, an Arctic fjord system in Svalbard, *Polar Res.*, *21*(1), 133–166.

Thierry, V., E. de Boisseson, and H. Mercier (2008), Interannual variability of the Subpolar Mode Water properties over the Reykjanes Ridge during 1990–2006, *J. Geophys. Res.*, *113*, C04016, doi:10.1029/2007JC004443.

Zweng, M. M., and A. Munchow (2006), Warming and freshening of Baffin Bay, 1916–2003, *J. Geophys. Res.*, *111*, C07016, doi:10.1029/2005JC003093.